ATLAS CONF Note

ATLAS-CONF-2023-011

24th March 2023

Measurement of the centrality dependence of the dijet yield in p+Pb collisions at $\sqrt{s_{\mathrm{NN}}}$ = 8.16 TeV with the ATLAS detector

The ATLAS Collaboration

ATLAS has measured the dijet per-event yield of anti-k_t $R = 0.4$ jets at center-of-mass energy $\sqrt{s_{\mathrm{NN}}} = 8.16$ TeV in p+Pb collisions. The measurement was performed using 165 nb^{-1} of p+Pb data collected in 2016. This note presents the per-event yield of dijets in terms of kinematic variables that allow for full characterization of the partonic scattering system, i.e. the average p_{T} of the dijet, $p_{\mathrm{T,Avg}} = (p_{\mathrm{T},1} + p_{\mathrm{T},2})/2$, the boost of the dijet system, $y_{\mathrm{b}} = (y_1^{\mathrm{CM}} + y_2^{\mathrm{CM}})/2$, and the half rapidity separation between the jets, $y^* = |y_1^{\mathrm{CM}} - y_2^{\mathrm{CM}}|/2$. The central-to-peripheral ratio of the dijet per-event yield in central and peripheral p+Pb collisions, R_{CP}, is constructed. The R_{CP} shows a clear dependence on the Bjorken-x of the parton extracted from the proton in the hard-scattering while no clear trend is observed when displaying the results as a function of the x of the parton extracted from the lead nucleus. These results will help the understanding of the effects introduced by the initial state kinematics on dijet production in p+Pb collisions.

ATLAS-CONF-2023-011
31 March 2023

1 Introduction

Proton-lead (p+Pb) collisions at the Large Hadron Collider (LHC) represent the current frontier for studying nuclear targets via hard-scattering of beams at the TeV scale [1]. The study of these reactions has the potential to elucidate the partonic composition of matter over a wide parton fractional momenta (x) range, covering from small-x ($\sim 10^{-4}$), where the onset of gluon saturation is predicted by certain models [2], up to the valence region. In addition, analysis of p+Pb data allows for the study of violations of the QCD factorization between hard and soft processes, which may be enhanced in scatterings involving nuclei, and can be used to investigate modifications of parton distribution functions (PDFs) in the nuclear environment [3–6].

Previously, ATLAS analyzed the centrality and rapidity dependence of inclusive jet production in 27.8 nb^{-1} of p+Pb collisions at $\sqrt{s_{\mathrm{NN}}}$ = 5.02 TeV [7]. The double-differential per-collision jet yield was measured as a function of jet rapidity (y) and transverse momentum (p_{T}) and compared between different centrality classes. The analysis reported a significant suppression of the jet production in central events compared to peripheral events at all p_{T} at forward rapidities and for large p_{T} at mid-rapidity. The suppression was found to be a function of only the total jet energy, suggesting that the observed violations may be directly related to the kinematics of the hard parton-parton scattering. A similar observation was made at RHIC [8].

Several competing interpretations were proposed for these findings. For example, the results were interpreted as an evidence that protons containing a parton with large x interact with a nuclear target with a significantly smaller than average cross-section and have smaller than average size [9]. Alternatively, other authors have suggested that in the constituent nucleon-nucleon collisions, energy production at backward rapidities decreases with increasing x in the proton-going direction, either via suppression of soft gluons available for particle production [10] or from an energy-momentum conservation between the hard process and the production of soft particles [11]. In general, the estimates of the collisions geometry in p+Pb collisions characterized by the presence of a hard scattering are expected to be affected by the modification of the soft particle production in nucleon-nucleon collisions [12, 13]. Motivated by some of the above arguments, a further measurement was performed to investigate how the forward transverse energy (E_{T}) production depends on parton-level kinematics just in proton-proton collisions in ATLAS [14], where the sum of E_{T} deposited in the calorimeter at large pseudorapidity in 2.76 TeV pp collisions is characterized in terms of the kinematics of dijet events.

ATLAS also analyzed dijet production in 360 μb^{-1} of p+Pb collisions at $\sqrt{s_{\mathrm{NN}}}$ = 5.02 TeV [15], focusing on forward-forward and forward-central angular correlations and conditional yields to search for the onset of gluon saturation effects enhanced by the nuclear environment [16]. This analysis found no significant broadening of the azimuthal correlations of dijets in p+Pb compared to pp collisions, and suppression of about 20% of the conditional yield of forward-forward dijets, which is not dependent on the transverse momentum of the leading or sub-leading jet. The statistics used in this analysis were not enough to allow for a measurement of the dijet conditional yield as a function of centrality.

The analysis presented in this note is based on 165 nb^{-1} of p+Pb collisions at $\sqrt{s_{\mathrm{NN}}}$ = 8.16 TeV collected in 2016. This data-set is of substantially higher integrated luminosity compared to previous p+Pb data-sets at the LHC. Dijet events, defined using the two highest transverse momentum jets in a given collision, are measured over a wide range of transverse momentum and rapidity[1] to carry out a detailed study of the triple-differential per-event dijet yield as a function of the collision centrality. The centrality of

[1] ATLAS uses a right-handed coordinate system with its origin at the nominal interaction point (IP) in the centre of the detector and the z-axis along the beam pipe. The x-axis points from the IP to the centre of the LHC ring, and the y-axis points upwards. Cylindrical coordinates (r, ϕ) are used in the transverse plane, ϕ being the azimuthal angle around the z-axis. The pseudorapidity is defined in terms of the polar angle θ as $\eta = -\ln\tan(\theta/2)$. The rapidity is defined as $y = \frac{1}{2}\ln[(E + p_z)/(E - p_z)]$, where E is the energy of a particle and p_z is the momentum component in the beam direction.

p+Pb collisions was characterized using the total transverse energy registered in the forward lead-going direction [17]. Whereas, in ion-ion collisions the interpretation of centrality immediately relates to the degree of nuclear overlap between the colliding nuclei, centrality in p+Pb collisions is sensitive to the number of interactions between the proton and nucleons bound in the lead nucleus.

The per-event dijet yield is measured as a function of

$$p_{\mathrm{T,Avg}} = \frac{p_{\mathrm{T},1} + p_{\mathrm{T},2}}{2}, \quad y_{\mathrm{b}} = \frac{y_1^{\mathrm{CM}} + y_2^{\mathrm{CM}}}{2}, \quad \text{and} \quad y^* = \frac{|y_1^{\mathrm{CM}} - y_2^{\mathrm{CM}}|}{2}, \tag{1}$$

where $p_{\mathrm{T,Avg}}$, y_{b}, and y^* are the average transverse momentum, the boost, and the half rapidity separation of the dijet system, respectively. The superscript CM denotes variables translated in the center of mass frame of the collision, while the subscripts '1' and '2' refer to the jets with the highest and second-highest p_{T} in a given event, respectively. These variables were chosen to provide results that fully constrain the partonic process kinematics:

$$x_p = \frac{p_{\mathrm{T},1} e^{y_1^{\mathrm{CM}}} + p_{\mathrm{T},2} e^{y_2^{\mathrm{CM}}}}{\sqrt{s}} \simeq \frac{2 p_{\mathrm{T,Avg}}}{\sqrt{s}} e^{y_b} \cosh(y^*), \tag{2}$$

$$x_{\mathrm{Pb}} = \frac{p_{\mathrm{T},1} e^{-y_1^{\mathrm{CM}}} + p_{\mathrm{T},2} e^{-y_2^{\mathrm{CM}}}}{\sqrt{s}} \simeq \frac{2 p_{\mathrm{T,Avg}}}{\sqrt{s}} e^{-y_b} \cosh(y^*), \tag{3}$$

$$m_{12} = \sqrt{x_p x_{\mathrm{Pb}} s} \simeq 2 p_{\mathrm{T,Avg}} \cosh(y^*), \tag{4}$$

where m_{12} represents the mass of the dijet system and x_p and x_{Pb} are the momentum fractions carried by the partons participating in the hard scattering, which originate from the colliding proton and the lead nucleus, respectively. Note that the measurement is not performed directly in these variables, but bins defined for the analysis can be approximately mapped to them using average kinematic values, as detailed in Section 6.

The triple differential per-event dijet yield was measured in different centrality classes:

$$\frac{1}{N_{\mathrm{evt}}^{\mathrm{cent}}} \frac{d^3 N_{\mathrm{dijet}}^{\mathrm{cent}}}{dp_{\mathrm{T,Avg}} dy_{\mathrm{b}} dy^*}, \tag{5}$$

where $N_{\mathrm{evt}}^{\mathrm{cent}}$ and $N_{\mathrm{dijet}}^{\mathrm{cent}}$ represent the number of sampled minimum bias and dijet events in the considered centrality interval, respectively. The centrality dependence of the per-event dijet yield was evaluated by constructing the central-to-peripheral ratio

$$R_{\mathrm{CP}}^{\frac{0\text{–}20\%}{60\text{–}90\%}}(p_{\mathrm{T,Avg}}, y_{\mathrm{b}}, y^*) = \frac{\frac{1}{\langle T_{\mathrm{AB}}^{0\text{–}20\%} \rangle} \frac{1}{N_{\mathrm{evt}}^{0\text{–}20\%}} \frac{d^3 N_{\mathrm{dijet}}^{0\text{–}20\%}}{dp_{\mathrm{T,Avg}} dy_{\mathrm{b}} dy^*}}{\frac{1}{\langle T_{\mathrm{AB}}^{60\text{–}90\%} \rangle} \frac{1}{N_{\mathrm{evt}}^{60\text{–}90\%}} \frac{d^3 N_{\mathrm{dijet}}^{60\text{–}90\%}}{dp_{\mathrm{T,Avg}} dy_{\mathrm{b}} dy^*}}, \tag{6}$$

where T_{AB} represents the nuclear thickness function [18], evaluated for different centralities, and 0–20% and 60–90% are the intervals used to define central and peripheral collisions, respectively. The R_{CP} is sensitive to modifications in the dijet rate from the geometric expectation between the p+Pb centralities.

2 ATLAS detector

The measurement presented in this paper is performed using the ATLAS calorimeter, inner detector, trigger, and data acquisition systems [19]. An extensive software suite [20] is used in the reconstruction and analysis of real and simulated data, in detector operations, and in the trigger and data acquisition systems of the experiment.

The calorimeter system consists of a sampling liquid-argon (LAr) electromagnetic (EM) calorimeter covering $|\eta| < 3.2$, a steel–scintillator sampling hadronic calorimeter covering $|\eta| < 1.7$, LAr hadronic calorimeters covering $1.5 < |\eta| < 3.2$, and two LAr forward calorimeters (FCal) covering $3.2 < |\eta| < 4.9$. The EM calorimeters are segmented longitudinally in shower depth into three layers with an additional presampler layer covering $|\eta| < 1.8$. The hadronic calorimeters have three sampling layers longitudinal in shower depth in $|\eta| < 1.7$ and four sampling layers in $1.5 < |\eta| < 3.2$, with a slight overlap in η. During the 2016 p+Pb Run, a sector of the hadronic endcap calorimeter (HEC), corresponding to $1.5 < \eta < 3.2$ and $-\pi < \phi < -\pi/2$ was disabled.

The inner detector measures charged particles within the pseudorapidity interval $|\eta| < 2.5$ using a combination of silicon pixel detectors, silicon microstrip detectors (SCT), and a straw-tube transition radiation tracker (TRT), all immersed in a 2 T axial magnetic field [19]. Each of the three detectors is composed of a barrel and two symmetric endcap sections. The pixel detector is composed of four layers including the insertable B-layer [21, 22]. The SCT barrel section contains four layers of modules with sensors on both sides, and each endcap consists of nine layers of double-sided modules with radial strips. The TRT contains layers of staggered straws interleaved with the transition radiation material.

ATLAS uses a two-level trigger system. The first-level trigger (Level 1) is hardware-based and implemented with custom electronics. It is followed by the software-based high-level trigger (HLT) [23].

3 Data selection and Monte Carlo

For the 2016 p+Pb run at $\sqrt{s_{\mathrm{NN}}} = 8.16$ TeV, the LHC beam energy configuration was asymmetric between the protons, 6.5 TeV, and the Pb nuclei, 2.5 TeV/nucleon, corresponding to a rapidity shift of the center of mass by 0.465 units toward the proton-going direction. The data were collected over two running periods characterized by opposite beam directions. In the first period of the data-taking, when lead ions (protons) circulated clockwise (counterclockwise) in the LHC, a total integrated luminosity of 57 nb^{-1} was collected. For the second period of data-taking, comprising a total integrated luminosity of 108 nb^{-1}, the direction of the two beam species was interchanged. The data analyzed in this note are comprised of both periods of data-taking, usually referred to as p+Pb and Pb+p orientations, respectively. The boost of the dijet system, y_{b}, is defined so that $y_{\mathrm{b}} > 0$ always refers to the proton-going direction.

The p+Pb data at $\sqrt{s_{\mathrm{NN}}} = 8.16$ TeV used in this analysis were required to satisfy detector and data-quality requirements, as well as to contain at least one reconstructed primary vertex and two reconstructed jets. The leading jet, defined as the reconstructed jet with the highest p_{T} in the event, was required to have passed the fully efficient[2] HLT chosen for the (η,p_{T}) region where the jet was detected, which sampled the largest luminosity. A set of central and forward single-jet triggers [23], characterized by different p_{T} thresholds, were chosen to provide full p_{T} coverage over a wide pseudorapidity range, corresponding to -3.1 $< \eta <$ 4.5 [3].

[2] In this analysis, a trigger is considered to be fully efficient if both HLT and Level 1 trigger efficiencies are greater than 99%.

[3] The given range is for the reference system where the proton is travelling toward positive η.

A minimum bias (MB) trigger, fully efficient for events containing at least one reconstructed primary vertex, was used to extend the phase space of the measurement down to $p_{\mathrm{T}} > 30$ GeV in both the forward and central region. The leading (sub-leading) jet was required to have $p_{\mathrm{T}} > 30$ (25) GeV. Events characterised by either the leading or the sub-leading jet in the acceptance of the disabled HEC region were discarded. In order to define a rejection criteria for the analysis, the disabled region was increased by an additional 0.4 margin in both pseudorapidity and azimuthal angle. In this way, jets with constituents affected by the disabled HEC are not considered.

The centrality of the p+Pb events used in the analysis was defined by the total transverse energy in the Pb-going FCal, $\Sigma E_{\mathrm{T}}^{\mathrm{Pb}}$ [17, 24]. The $\Sigma E_{\mathrm{T}}^{\mathrm{Pb}}$ distribution for MB p+Pb collisions is shown in Figure 1. Pile-up events are rejected by requiring any other vertex than the primary to have less than 7 associated tracks. The leading and sub-leading jets were required to be at least 0.4 pseudorapidity units away from the Pb-going FCal arm to reject events with biased centrality. The centrality intervals were defined in terms of percentiles of the $\Sigma E_{\mathrm{T}}^{\mathrm{Pb}}$; the following centrality classes were used in this analysis, 0–20%, and 60–90%. Background contributions to jet production from ultra-peripheral collisions were estimated through a study which used rapidity gap selections and were found to have a negligible contribution to the 0–90% centrality interval. Therefore, by only considering events with centrality in this interval, dijet events associated to ultra-peripheral collisions are effectively rejected. The nuclear thickness function, T_{AB}, was calculated in each centrality interval using the Glauber Monte Carlo (MC) [25, 26].

This analysis used MC simulations to evaluate the performance of the detector and analysis procedure, and to correct the measured distributions for detector effects. The detector response in all MC samples was simulated using GEANT4 [27, 28]. The HEC issue is replicated at the level of reconstruction in the simulation. The p+Pb MC sample makes use of dijet events from 8.16 TeV pp collisions, including the boost in rapidity with respect to the lab frame that is in the data, simulated by PYTHIA8 [29] with the A14 set of tuned parameters [30] and the NNPDF2.3LO parton distribution functions [31]. Events from the PYTHIA8 dijet sample were overlayed with events from a dedicated sample of p+Pb data events. The overlay procedure combines the PYTHIA8 and data events during the digitization step of simulation. A separate overlay MC sample was produced for each beam configuration. These MC overlay samples were reweighted on an event-by-event basis such that they have the same $\Sigma E_{\mathrm{T}}^{\mathrm{Pb}}$ distribution as the data samples to better represent the centrality distribution. Additionally, a 10M event dijet sample was generated using Herwig7 [32] in order to study the flavor component of the jet energy scale uncertainty.

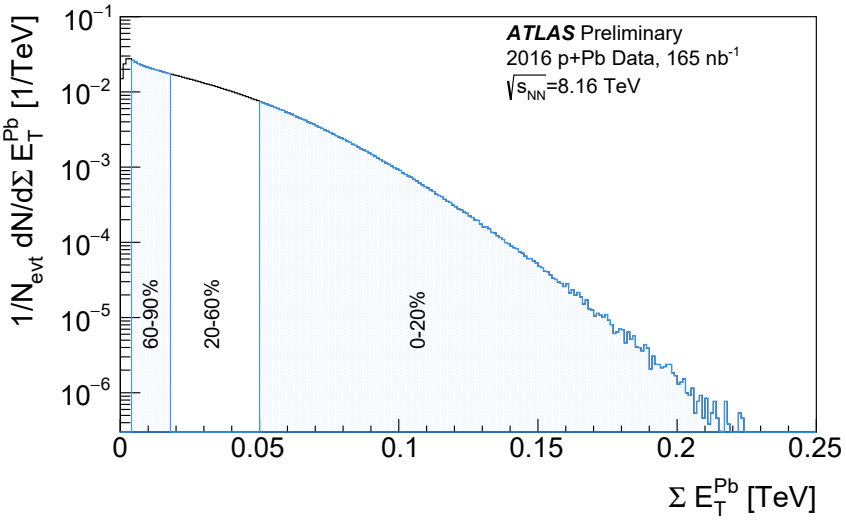

Figure 1: Distribution of $\Sigma E_{\mathrm{T}}^{\mathrm{Pb}}$ in MB p+Pb collisions at 8.16 TeV as a function of $\Sigma E_{\mathrm{T}}^{\mathrm{Pb}}$. The vertical divisions correspond to the centrality intervals defined for this analysis. From right to left, the regions correspond to centrality intervals of 0–20%, 20–60% and 60–90%.

4 Analysis

Similar to previous ATLAS jet measurements in p+Pb [33] and Pb+Pb [34] collisions, the jets used in this analysis were reconstructed using the anti-k_t algorithm [35] as implemented within the FastJet software package [36]. Jets with $R = 0.4$ were formed by clustering four vectors corresponding to massless calorimeter towers with size $\Delta\eta \times \Delta\phi = 0.1 \times (\pi/32)$. The background energy arising from the underlying event (UE) was subtracted from each tower. This step was accomplished by applying an iterative procedure that estimates the UE average transverse energy density, $\rho(\eta)$, while excluding regions of the detector populated by jets [37]. The UE evaluation was additionally corrected for η-ϕ dependent non-uniformities of the detector.

The jet reconstruction performance was characterized by evaluating the jet energy scale (JES) and resolution (JER), which correspond to the mean and variance of the $p_{\mathrm{T}}^{\mathrm{reco}}/p_{\mathrm{T}}^{\mathrm{truth}}$ distribution. In this formula, $p_{\mathrm{T}}^{\mathrm{reco}}$ represents the reconstructed jet p_{T} and $p_{\mathrm{T}}^{\mathrm{truth}}$ is the p_{T} of the matched generator-level jet, within $\Delta R < 0.3$. Generator-level jets were also built using the anti-k_t algorithm with $R = 0.4$, fed in as input the four-vectors of stable particles obtained from the Monte Carlo generator that are not muons or neutrinos. In this context, a particle is considered stable if it has a proper lifetime greater than 30 ps. Since the 2016 p+Pb data were collected using two different beam orientations, corresponding to a different energy density of the UE across the detector, as well as different relevance of specific detector inefficiencies, the JES and JER were evaluated separately for each beam configuration. Figures 2 and 3 show the JES and JER as a function of $p_{\mathrm{T}}^{\mathrm{truth}}$ for p+Pb and Pb+p collisions, respectively.

The jet reconstruction efficiency for jets with $p_T^{\mathrm{reco}} > 5$ GeV was also studied using Monte Carlo simulations. The results are demonstrated in Figures 4 and 5 and show that the jet reconstruction efficiency is greater than 99% in all η regions considered for the analysis for $p_{\mathrm{T}}^{\mathrm{truth}} > 25$ GeV. The JES deviates from unity by up to 3% at low p_{T} in the forward region. The worsening of the JER in the forward proton-going η region for each of the beam orientations was also observed in previous analyses, see for instance Ref. [38]. The

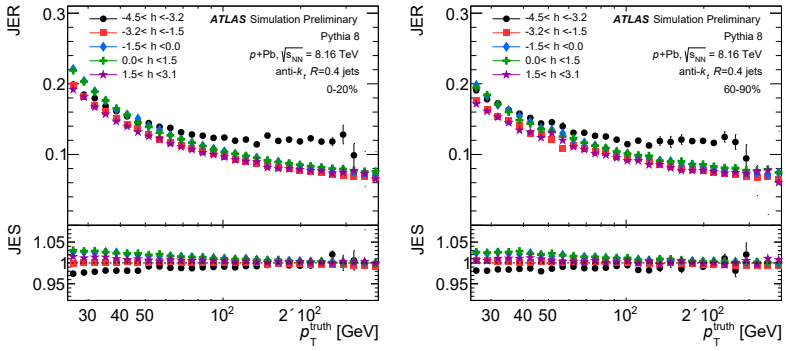

Figure 2: Jet energy resolution (top) and jet energy scale (bottom) evaluated in p+Pb collisions (p traveling towards negative η) as a function of $p_{\mathrm{T}}^{\mathrm{truth}}$, different η of the leading jet, and for different p+Pb centrality classes.

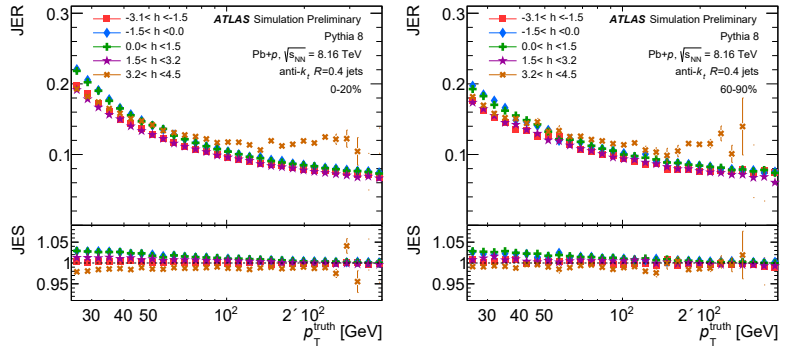

Figure 3: Jet energy resolution (top) and jet energy scale (bottom) evaluated in Pb+p collisions (p traveling towards positive η) as a function of $p_{\mathrm{T}}^{\mathrm{truth}}$, different η of the leading jet, and for different p+Pb centrality classes.

origin of this effect is the transition between the central and forward calorimeters. Those two systems are characterized by different calorimeter geometry and technology, resulting in different responses that alter the reconstructed four-momentum [39]; all the JES and JER-related effects were corrected for by the unfolding procedure discussed below.

This analysis considered the measured dijet pair constructed from the two highest p_{T} jets in the event with reconstructed $p_{\mathrm{T},1} > 30$ GeV, $p_{\mathrm{T},2} > 25$ GeV and $-4.5 < \eta < 2.8$ ($-2.8 < \eta < 4.5$) for the p+Pb (Pb+p) beam orientation. The backward η cut was imposed to avoid jets biasing the centrality determination in the Pb-going arm of the FCal. This choice effectively reduced the fiducial acceptance of the measurement at backward y_{b}. The measurement utilizes logarithmic binning from 30 – 1000 GeV in $p_{\mathrm{T,Avg}}$ with linear binning in y_{b} and y^{*}, from -3.0 – 4.5 and 0.0 – 4.5, respectively.

To correct for detector effects and bin migration due to finite jet energy resolution, the per-event dijet yield was unfolded in $p_{\mathrm{T,Avg}}$ using a one-dimensional Bayesian procedure [40] with three iterations, implemented within the RooUnfold package [41]. For each y_{b}, y^{*}, and centrality bin, a response matrix was filled using truth-reconstructed pairs of jets from the Pythia8 sample overlaid with minimum-bias p+Pb data. An efficiency correction was included in the unfolding to account for reconstructed jets that migrate out of the measurement phase space at the detector-level due to energy resolution effects, as well as the disabled HEC region. The size of the efficiency correction on the yields related to the disabled HEC is significant only in the corresponding pseudorapidity region, where it reaches approximately a factor of three.

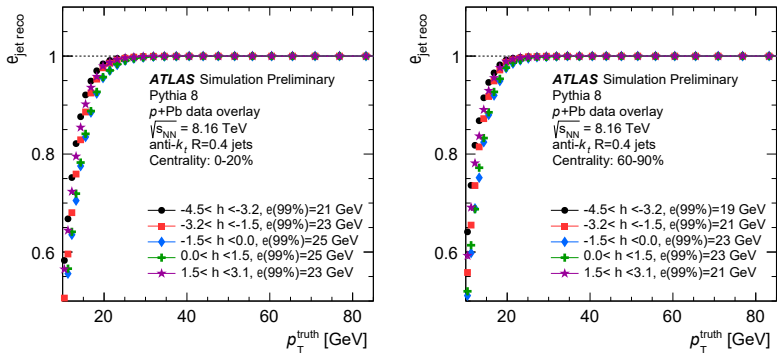

Figure 4: Jet reconstruction efficiency in p+Pb data-taking configuration, evaluated in different η regions of the ATLAS detector for central (0–20%, left) and peripheral (60–90%, right) collisions. All jets with p_T^{reco}>5 GeV were considered in these studies. Corresponding 99% efficiency $p_{\text{T}}^{\text{truth}}$ thresholds are also reported for each η region and centrality interval.

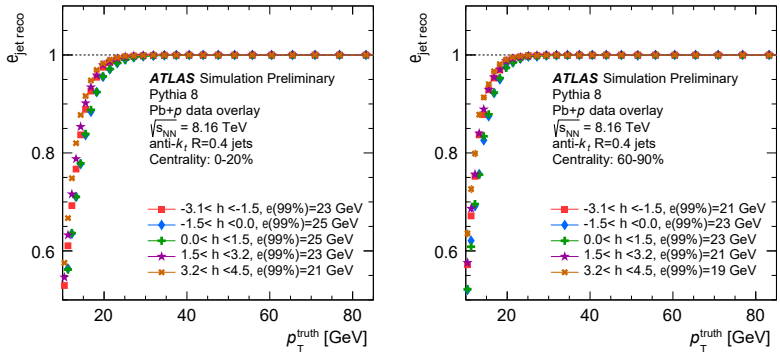

Figure 5: Jet reconstruction efficiency in Pb+p data-taking configuration, evaluated in different η regions of the ATLAS detector for central (0–20%, left) and peripheral (60–90%, right) collisions. All jets with p_T^{reco}>5 GeV were considered in these studies. Corresponding 99% efficiency $p_{\text{T}}^{\text{truth}}$ thresholds are also reported for each η region and centrality interval.

The response matrices used in the unfolding procedure are binned uniformly in the logarithm of $p_{\text{T,Avg}}$. Additionally, the truth $p_{\text{T,Avg}}$ response binning includes underflow and overflow bins to allow for reconstructed jet pairs with truth $p_{\text{T,Avg}}$ below, or above, the kinematic selection to migrate out of the measurement region. There is no significant migration across y_{b} or y^* in this measurement. Each response matrix was reweighted at the event level by the ratio of reconstructed data to reconstructed Monte Carlo, such that the Monte Carlo spectrum better matches the shape of the data. The unfolding was performed using three iterations, which has been selected to minimize the statistical uncertainty and relative bin migration after each iteration. The statistical uncertainty on the yield was evaluated using a bootstrapping method [42].

To properly unfold for the detector effects, the data from the two running periods were analyzed separately using dedicated simulations for each beam orientation. In order to combine the two beam orientations, after unfolding, results obtained from data collected with the p beam travelling towards negative rapidities are flipped in y_{b} to obtain a reference system compatible with the data where the p is travelling towards positive rapidities. After this step, the final yield was obtained by calculating the statistical-weighted mean of the two periods. The R_{CP} was then derived according to Equation 6, where the 60–90% centrality bin serves as the reference, and the 0–20% is used to represent central dijet events.

5 Systematic uncertainties

The per-event dijet yield is subject to systematic uncertainties associated with the jet energy scale and resolution, the unfolding procedure, and a systematic uncertainty due to a sector of the HEC being disabled for the running period. An additional systematic uncertainty on the T_{AB} modeling was considered for the R_{CP} measurement. For each source of systematic uncertainty, except for the uncertainty on the disabled HEC sector and the T_{AB}, the entire analysis is repeated by varying the response matrix according to the systematic variation. The difference between the nominal measurement and that obtained with the systematic variation is taken as the estimate of the systematic uncertainty.

The JES uncertainty for this analysis has three components. The first was evaluated using *in situ* studies of the calorimeter response of jets reconstructed with the procedure used in 13 TeV pp collisions [43]. A second component accounts for the relative energy scale difference between the jet reconstruction procedures used in this analysis and those in 13 TeV pp collisions [44]. The third JES component accounts for potential inaccuracies in the Monte Carlo sample's description of the relative abundances of jets initiated by quarks and gluons and of the calorimetric response to quark and gluon jets. Two Monte Carlo generators, namely Pythia8 and Herwig7, were used to evaluate the magnitude of the third JES component. To account for the uncertainty on the JES in the dijet measurement, each component was varied separately by ± 1 standard deviation in the Monte Carlo sample, applied as a function of p_{T} and η, and the response matrices were recomputed. The data were then unfolded with the modified matrices. The JES is the dominant systematic uncertainty, specifically the third component, in nearly every bin of the per-event dijet yield measurement. This systematic uncertainty is generally 10–15%, but cancels due to correlation in the R_{CP} measurement, where the JER is the dominant systematic contribution.

The uncertainty due to the JER was evaluated by applying a Gaussian smearing factor to the reconstructed jet p_{T} in the Monte Carlo sample, and producing modified response matrices. The smearing factor was taken from *in situ* studies of dijet energy balance [43]. An additional uncertainty was included to account for differences between the tower-based jet reconstruction and the jet reconstruction used in analyses of 13 TeV pp data, as well as differences in calibration procedures [44]. The resulting uncertainty from the JER was symmetrized, and is typically the sub-dominant systematic uncertainty, reaching up to $\sim$10%.

The systematic uncertainty on the unfolding is related to the sensitivity of the unfolding procedure to the choice of the input distribution. To determine the sensitivity of results to the reweighting procedure, the slope and intercept of the fit to the ratio of the detector-level spectrum in data to that in simulation was varied by the fit uncertainty, similarly to the approach used in Ref. [7]. A new set of response matrices was then generated using the alternative weighting and the full analysis procedure was repeated. The difference from the nominal result was taken as a systematic uncertainty and is at the sub-percent level for all bins.

Reconstructed level jets that fall within $R = 0.4$ of the region covered by the disabled HEC sector have been removed from the analysis. The systematic uncertainty associated with this removal was evaluated by increasing the exclusion region by 0.1 in all directions in azimuth and pseudorapidity, and repeating the analysis procedure. The difference between the nominal exclusion and increased exclusion was taken as a systematic uncertainty and is symmetrized. The resultant uncertainty was found to be on the order of 1-2% in the majority of the measurement's phase space. The uncertainty on the T_{AB} arises from the geometric modeling and the efficiency of the minimum-bias trigger. The T_{AB} uncertainty is only applicable to the R_{CP} measurement and is treated as correlated between central and peripheral T_{AB} entering the ratio. For the standard Glauber model, the uncertainty on the R_{CP} related to the T_{AB} determination has a value of +10% and −16% in all kinematic intervals used in the analysis.

For each systematic variation, the full analysis procedure was performed and the difference from the nominal result was taken as the uncertainty. The variations for each systematic uncertainty were then added in quadrature to produce the individual systematic uncertainties. For the R_{CP} measurement, the JES, JER, and HEC uncertainty were taken to be correlated. The partial cancellation of the resulting systematic uncertainties from correlated sources results in smaller uncertainties on the R_{CP} compared to those on the per-event dijet yield. The total systematic uncertainties on the 0–20% and 60–90% per-event dijet yield, and on the R_{CP} measurement are shown, for three representative bins of the measurement, in Figures 6, 7, and 8, respectively. A Gaussian smoothing has been applied to the systematic uncertainties, in order to minimize statistical fluctuations.

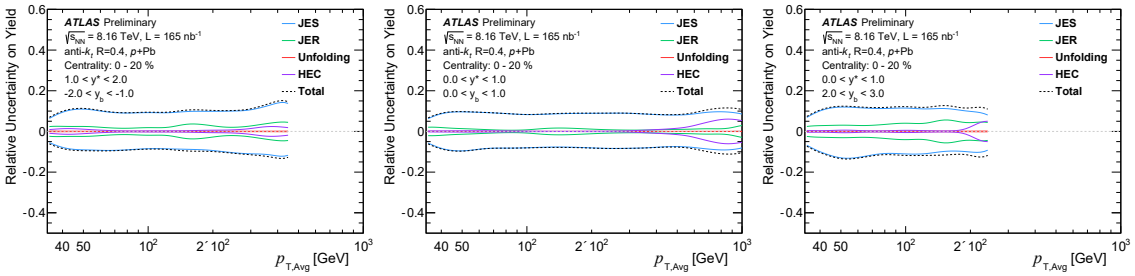

Figure 6: The systematic uncertainties on the 0–20% per-event dijet yield measurement as a function of $p_{\mathrm{T,Avg}}$ in three representative bins of y_{b} and y^* for $\sqrt{s_{\mathrm{NN}}}$ = 8.16 TeV p+Pb collisions. Each panel shows the total systematic uncertainty (black dashed line), as well as the contributions from each source, namely the JES, JER, unfolding and disabled HEC sector.

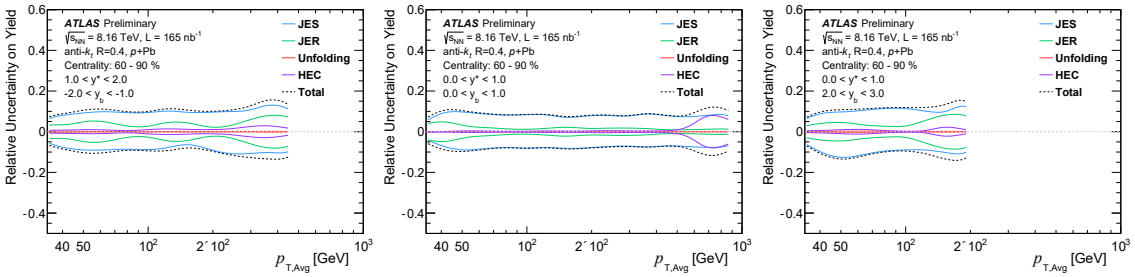

Figure 7: The systematic uncertainties on the 60–90% per-event dijet yield measurement as a function of $p_{\mathrm{T,Avg}}$ in three representative bins of y_{b} and y^* for $\sqrt{s_{\mathrm{NN}}}$ = 8.16 TeV p+Pb collisions. Each panel shows the total systematic uncertainty (black dashed line), as well as the contributions from each source, namely the JES, JER, unfolding and disabled HEC sector.

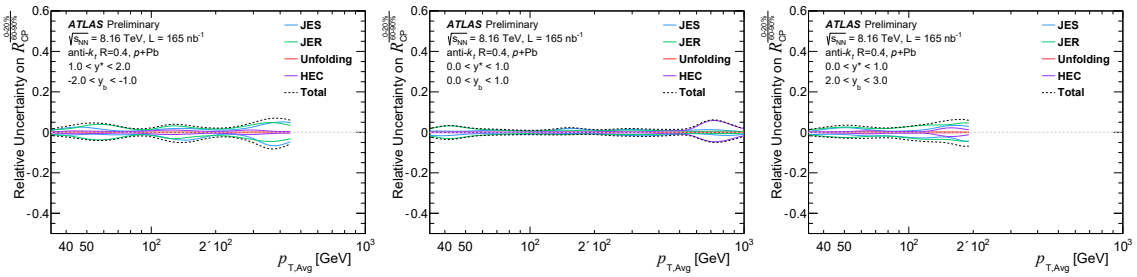

Figure 8: The systematic uncertainties on the R_{CP} measurement as a function of $p_{\mathrm{T,Avg}}$ in three representative bins of y_{b} and y^* for $\sqrt{s_{\mathrm{NN}}}$ = 8.16 TeV p+Pb collisions. Each panel shows the total systematic uncertainty (black dashed line), as well as the contributions from each source, namely the JES, JER, unfolding, and HEC sector exclusion. The T_{AB} uncertainty (not displayed) has a value of +10% and −16% in all bins.

6 Results

Figures 9 and 10 present the fully-corrected per-event dijet yield as a function of $p_{\mathrm{T,Avg}}$ in 0–20% and 60–90% p+Pb collisions, respectively, for each of the y_{b} and y^{*} ranges chosen for this analysis. At mid values of y_{b}, the yield spans over seven orders of magnitude. In each y_{b} bin, a decreasing trend in the yield with $p_{\mathrm{T,Avg}}$ and y^{*} is observed.

Results for the central-to-peripheral ratio, R_{CP}, for dijets in p+Pb collisions are summarized in Figure 11. The R_{CP} shows a suppression in the dijet yield measured in central p+Pb collisions compared to peripheral ones. The suppression is dependent on $p_{\mathrm{T,Avg}}$, y_{b}, and y^{*}. In all the y^{*} intervals studied, the R_{CP} decreases with increasing $p_{\mathrm{T,Avg}}$. Furthermore, in a given $p_{\mathrm{T,Avg}}$ and y_{b} interval, the R_{CP} decreases with y^{*}. In addition, the R_{CP} is found to decrease while moving from backward to forward y_{b} intervals in a given y^{*} region.

The results are mapped to the kinematics of the partonic system. The triple-differential analysis, as defined in Equation 1, allows for a fully constrained investigation of the partonic system via Equations 2, 3 and 4. A demonstration of the (x_p, x_{Pb}) coverage of each kinematic bin is shown in Figure 12. The corresponding $(y_1^{\mathrm{CM}}, y_2^{\mathrm{CM}})$ distribution for each kinematic bin is shown in Figure 13. Figures 12 and 13 were constructed using p+Pb data prior to unfolding.

Figures 14 and 15 show the R_{CP} of the per-event dijet yield as a function of the approximated x_p and x_{Pb}, respectively, for all the (y_{b}, y^{*}) bins utilized in the analysis. The approximation of the two partonic fractional momenta are constructed by re-scaling the central value of the $p_{\mathrm{T,Avg}}$ bin of each experimental point according to Equations 2 and 3, using the average $\langle y^{*} \rangle$ and $\langle y_{\mathrm{b}} \rangle$ values in the given kinematic bin. The results show that the observed suppression follows a log-linear trend starting from $x_p \sim 10^{-2}$ toward the valence region. When displayed as a function of x_{Pb}, a common trend is not present. A reduction of the R_{CP} is observed while moving from the valence (backward dijet boost) to the low-x (forward dijet boost) region. Within the same y_{b} bin, the results are found to follow a log-linear decrease from lower to higher values of x_{Pb}. The comparison of the two results suggests that the observed suppression of the R_{CP} may depend on the underlying parton kinematics and that the momentum of the parton extracted from the p beam may play a significant role in determining the per-event dijet yield in different centrality classes of p+Pb collisions. The results hint that the observed trend is governed by physics effects similar to those probed in the inclusive production of jets in p+Pb collisions at 5.02 TeV [7].

Figure 16 shows the results as a function of the approximated x_p for different selections of the approximated x_{Pb}. The log-linear decreasing trend in x_p is found to be mildly dependent on the x_{Pb} region probed in the collision. It is interesting to note how the log-linear trend begins to fade around $x_p \sim 10^{-2}$ when $5 \times 10^{-2} < x_{\mathrm{Pb}} < 2 \times 10^{-1}$, and is mostly gone when the R_{CP} is extracted for $x_{\mathrm{Pb}} > 2 \times 10^{-1}$. On the other hand, it is worth noting how the highest suppression is found to be associated to the lowest x_{Pb} selection. For completeness, Figure 17 presents the R_{CP} results in terms of the approximated mass of the dijet system, m_{12}. When displayed in terms of this variable, the R_{CP} shows a log-linear decreasing trend with slopes characteristic of each y_{b} bin.

These results are compatible with the physics model proposed in Ref. [9]. Arguments formulated in Refs. [10] and [11] are not directly in contradiction with the new results reported in this manuscript but, in their current formulation, they are disfavored by a previous ATLAS measurement of the relationship between jet production and the underlying event activity in large pseudorapidity-separated regions [14].

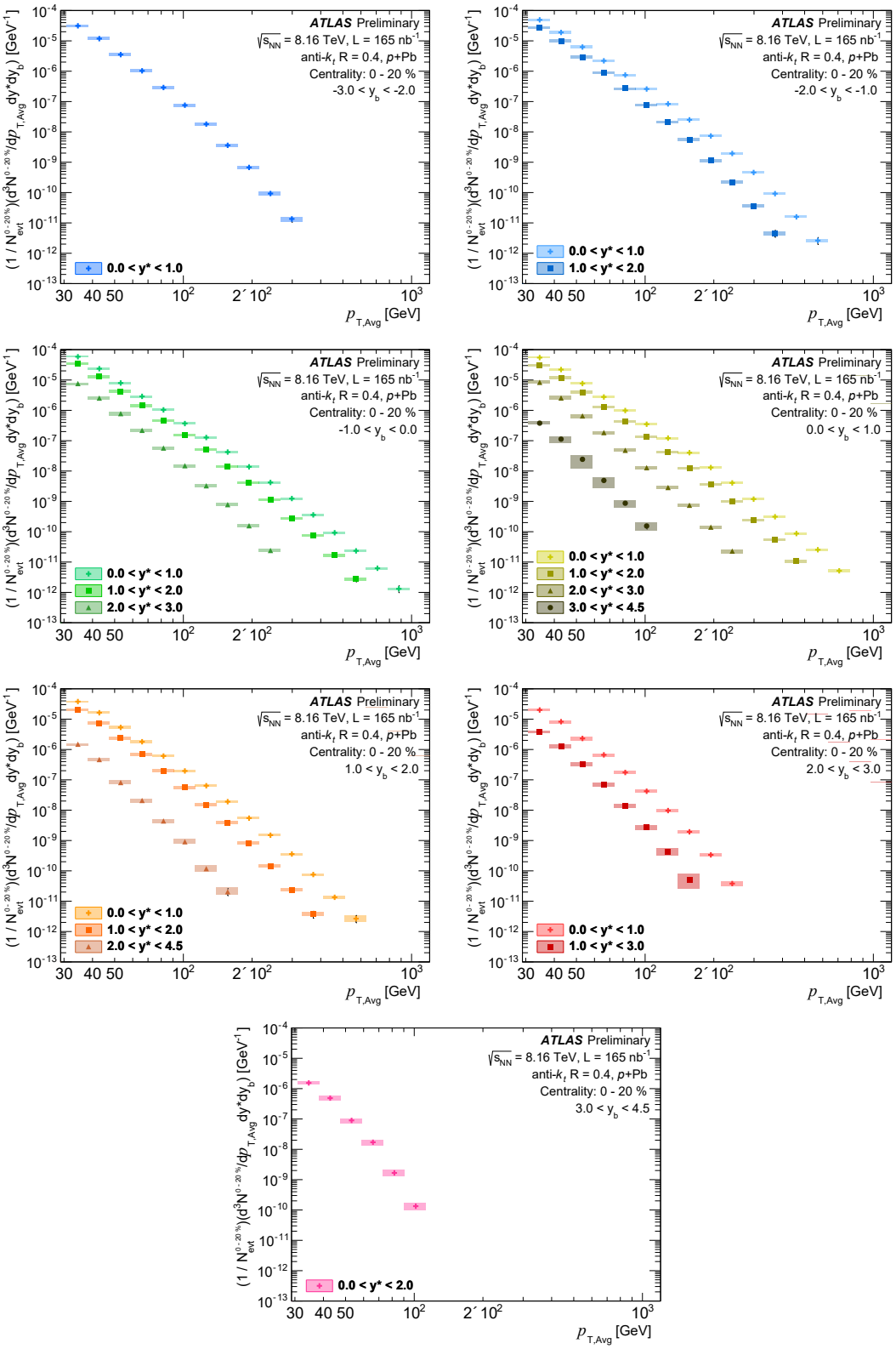

Figure 9: Triple differential per-event dijet yield in 0–20% p+Pb collisions as a function of $p_{\mathrm{T,Avg}}$. Each panel shows the results in different y^* intervals for a fixed y_{b} bin. Note that positive y_{b} corresponds to the proton-going direction. Colored rectangles represent the total systematic uncertainty, while the vertical black error bars represent the statistical uncertainty.

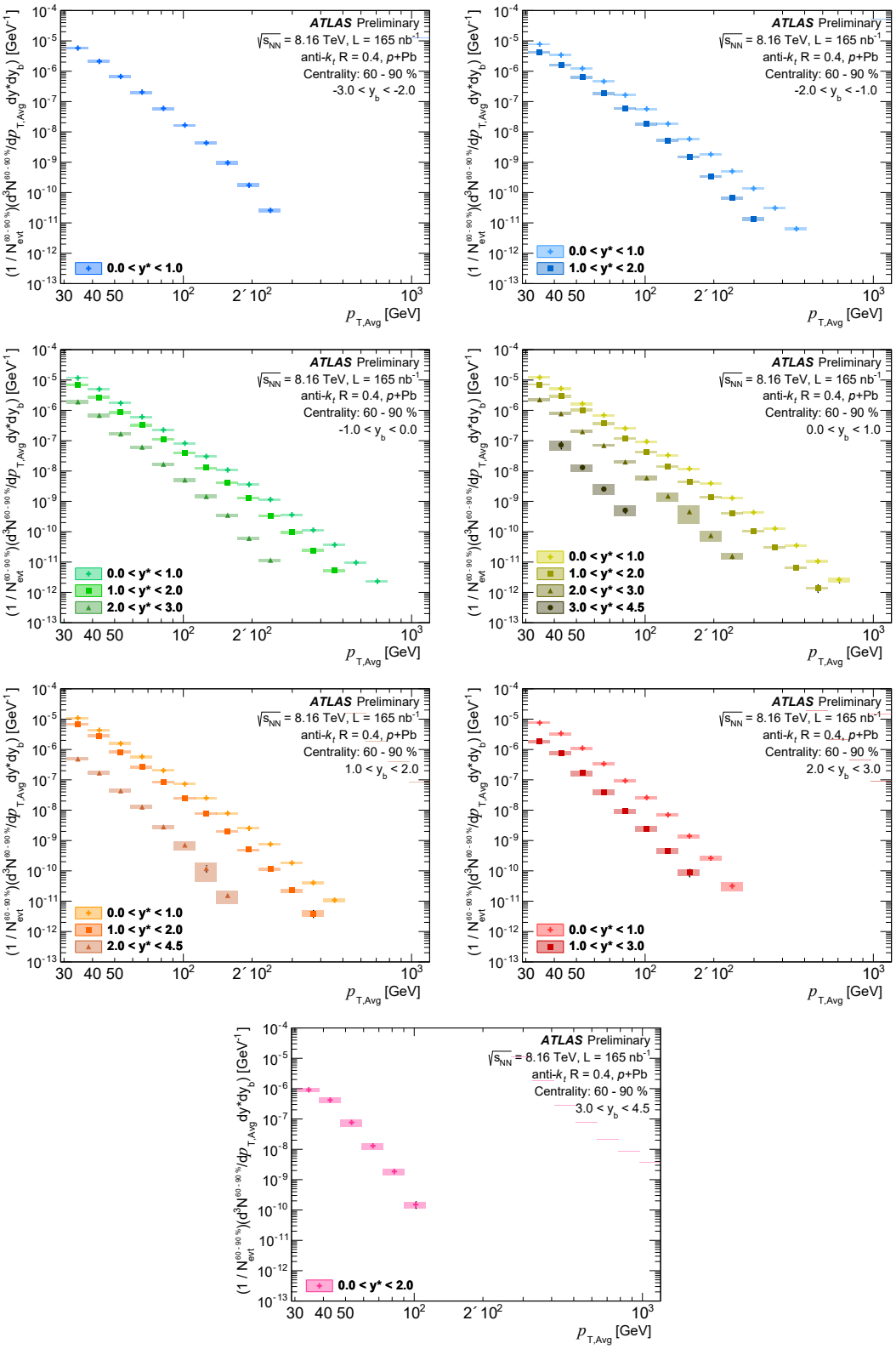

Figure 10: Triple differential per-event dijet yield in 60–90% p+Pb collisions as a function of $p_{\mathrm{T,Avg}}$. Each panel shows the results in different y^* intervals for a fixed y_{b} bin. Note that positive y_{b} corresponds to the proton-going direction. Colored rectangles represent the total systematic uncertainty, while the vertical black error bars represent the statistical uncertainty.

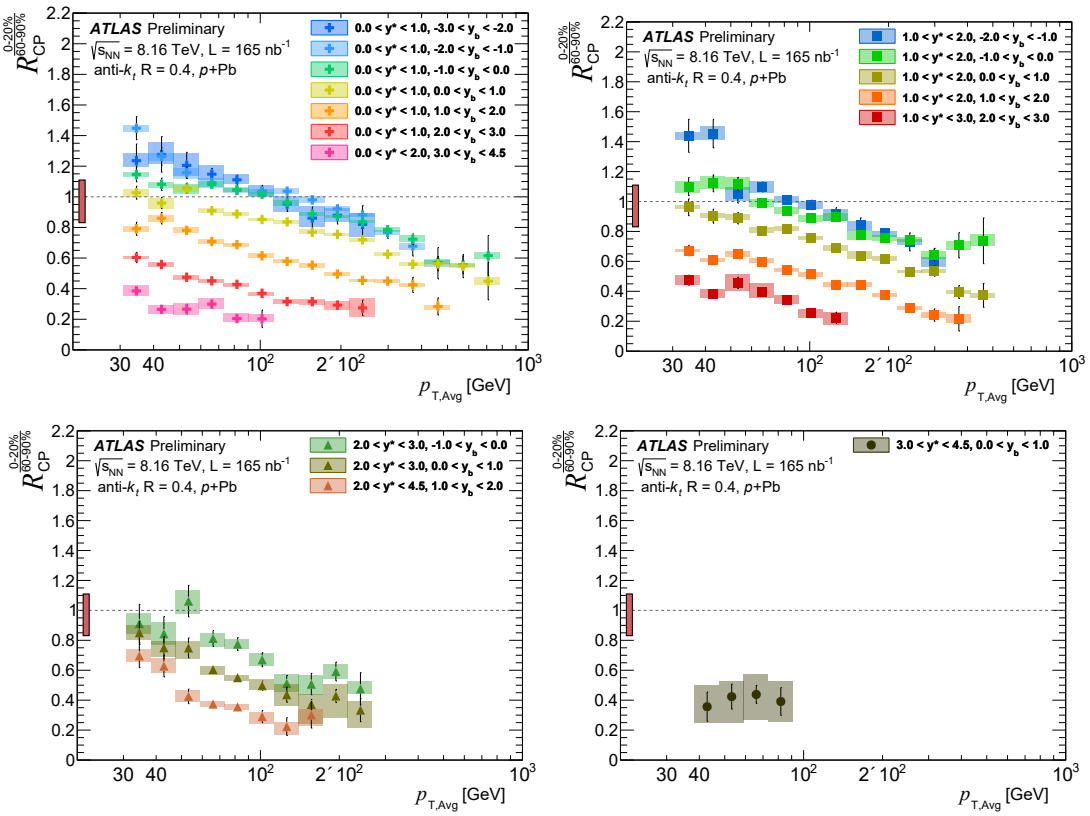

Figure 11: R_{CP} plotted as a function of the $p_{\mathrm{T,Avg}}$ in different y^* ranges, with the smallest separation in rapidity shown in the upper-left panel and the largest separation in rapidity shown in the bottom-right panel. Note that positive y_{b} corresponds to the proton-going direction. Colored rectangles represent the total systematic uncertainty, while the vertical black error bars represent the statistical uncertainty. The solid red rectangle on the left side of each panel represents the uncertainty on the T_{AB}.

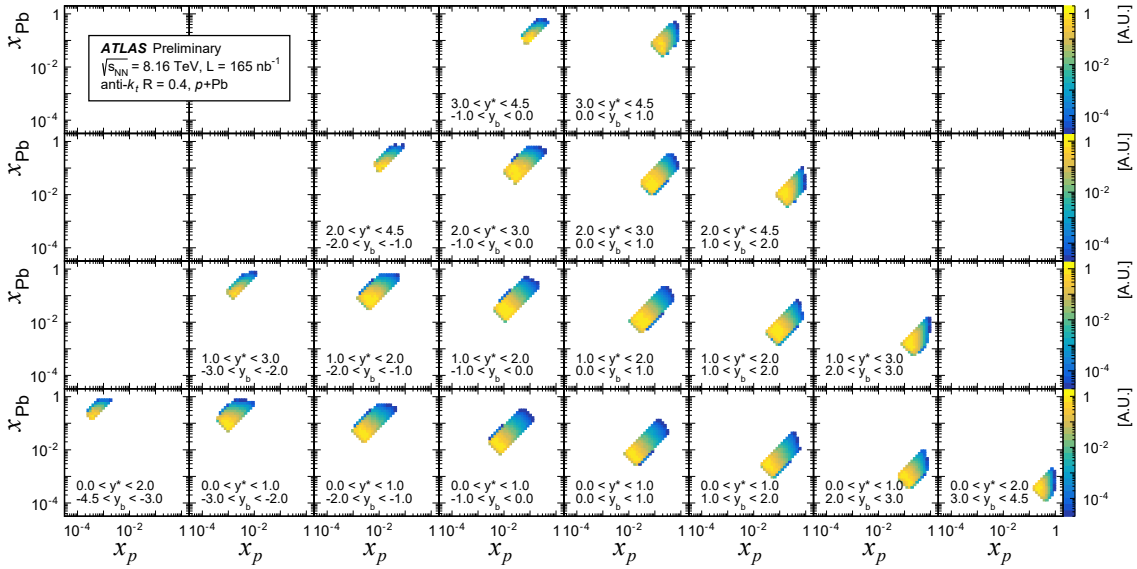

Figure 12: The distribution of x_{Pb} vs x_{p} for p+Pb data at 8.16 TeV, in bins of y_{b} and y^*. Positive y_{b} corresponds to the proton travelling towards positive rapidities. Each panel is self-normalized.

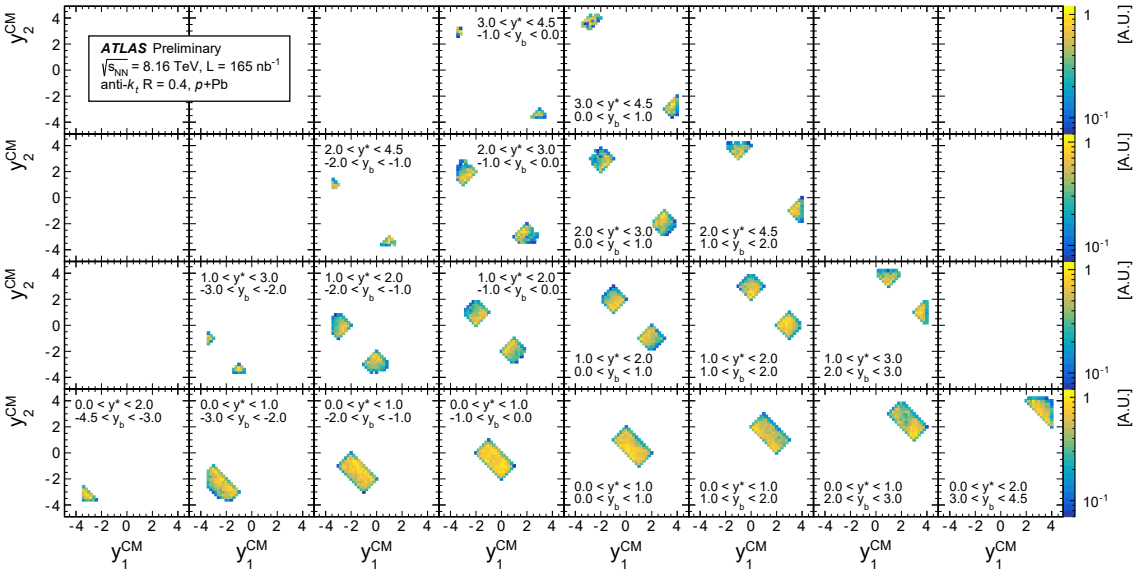

Figure 13: The distributions of y_1^{CM} vs y_2^{CM} for p+Pb data at 8.16 TeV, in bins of y_{b} and y^*. Positive y_{b} corresponds to the proton travelling towards positive rapidities. Each panel is self-normalized.

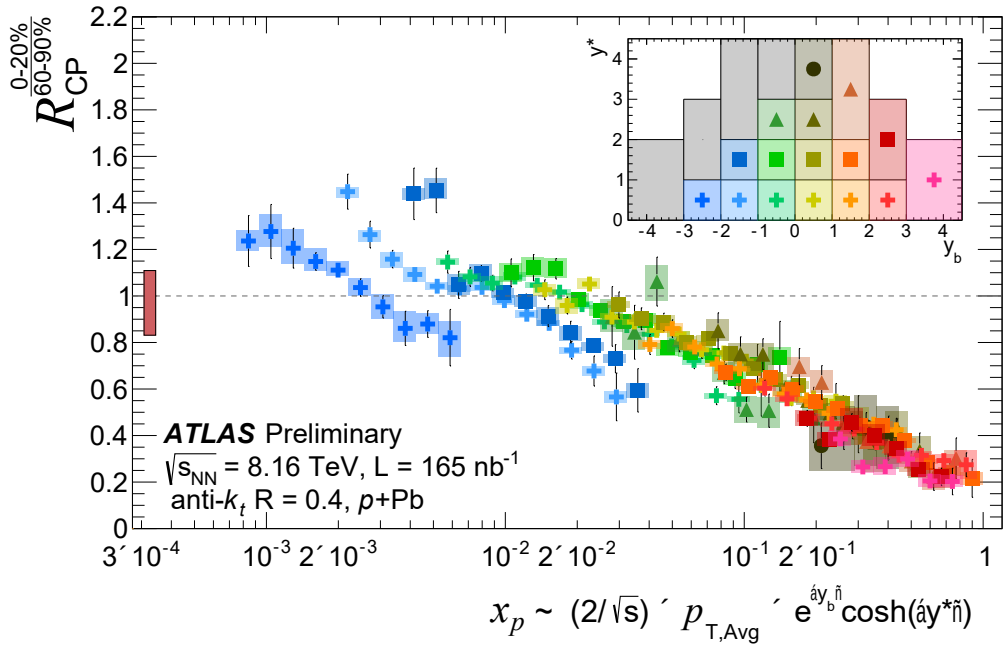

Figure 14: R_{CP} plotted as a function of approximated x_p, constructed using $\langle y_{\mathrm{b}} \rangle$ and $\langle y^* \rangle$. An inlay legend is included, showing the (y_{b}, y^*) bins, and their corresponding markers and colors. Note that positive y_{b} corresponds to the proton-going direction. Colored rectangles represent the total systematic uncertainty, while the vertical black error bars represent the statistical uncertainty. The solid red rectangle on the left-side of the panel represents the uncertainty on the T_{AB}. Four (y_{b}, y^*) bins, denoted in the legend by a grey color and no marker, were dropped from the analysis as the presence of jets in these intervals, which are nearby to the forward calorimeter, may bias the centrality determination.

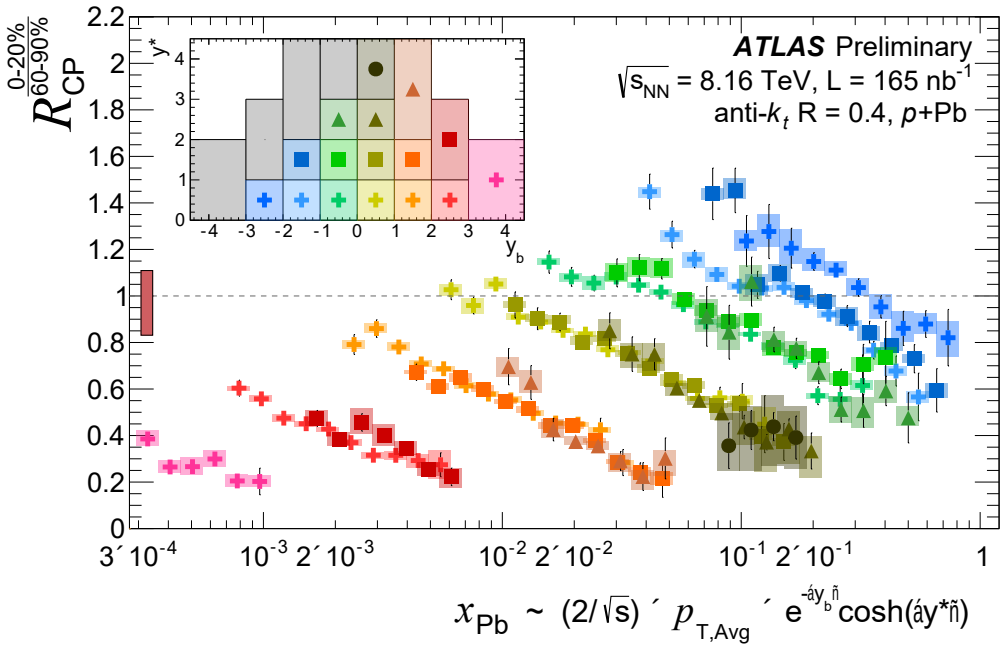

Figure 15: R_{CP} plotted as a function of approximated x_{Pb}, constructed using $\langle y_{\mathrm{b}} \rangle$ and $\langle y^{*} \rangle$. An inlay legend is included, showing the (y_{b}, y^{*}) bins, and their corresponding markers and colors. Note that positive y_{b} corresponds to the proton-going direction. Colored rectangles represent the total systematic uncertainty, while the vertical black error bars represent the statistical uncertainty. The solid red rectangle on the left-side of the panel represents the uncertainty on the T_{AB}. Four (y_{b}, y^{*}) bins, denoted in the legend by a grey color and no marker, were dropped from the analysis as the presence of jets in these intervals, which are nearby to the forward calorimeter, may bias the centrality determination.

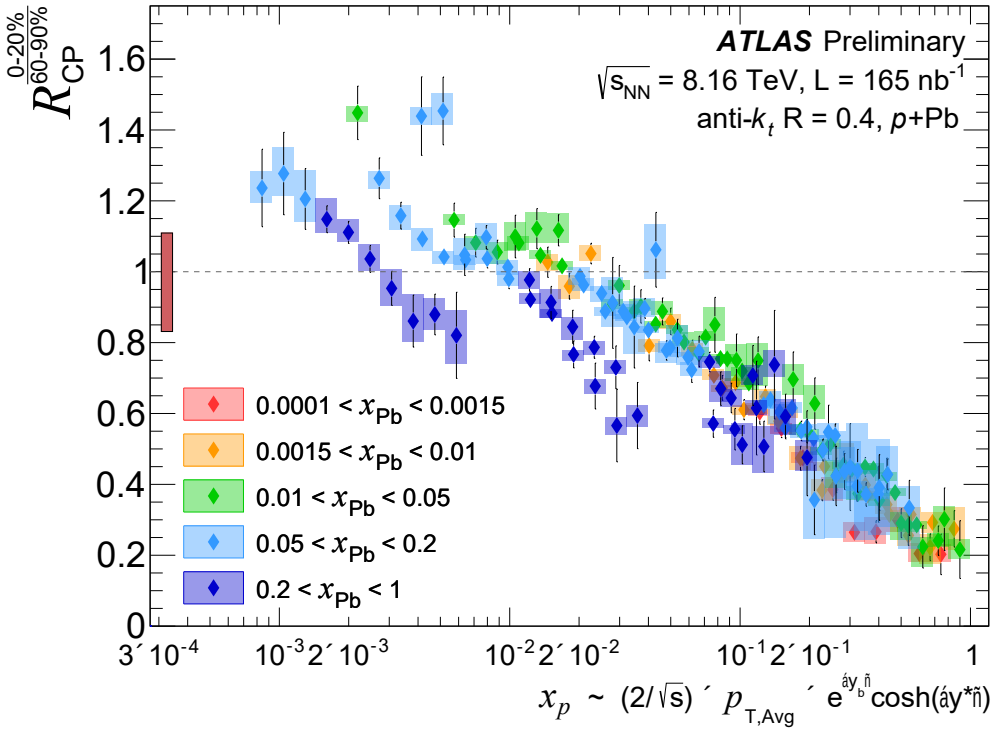

Figure 16: R_{CP} plotted as a function of approximated x_p, in different ranges of approximated x_{Pb}, both constructed using $\langle y_{\mathrm{b}} \rangle$ and $\langle y^* \rangle$. Note that positive y_{b} corresponds to the proton-going direction. Colored rectangles represent the total systematic uncertainty, while the vertical black error bars represent the statistical uncertainty. The solid red rectangle on the left side of the panel represents the uncertainty on the T_{AB}.

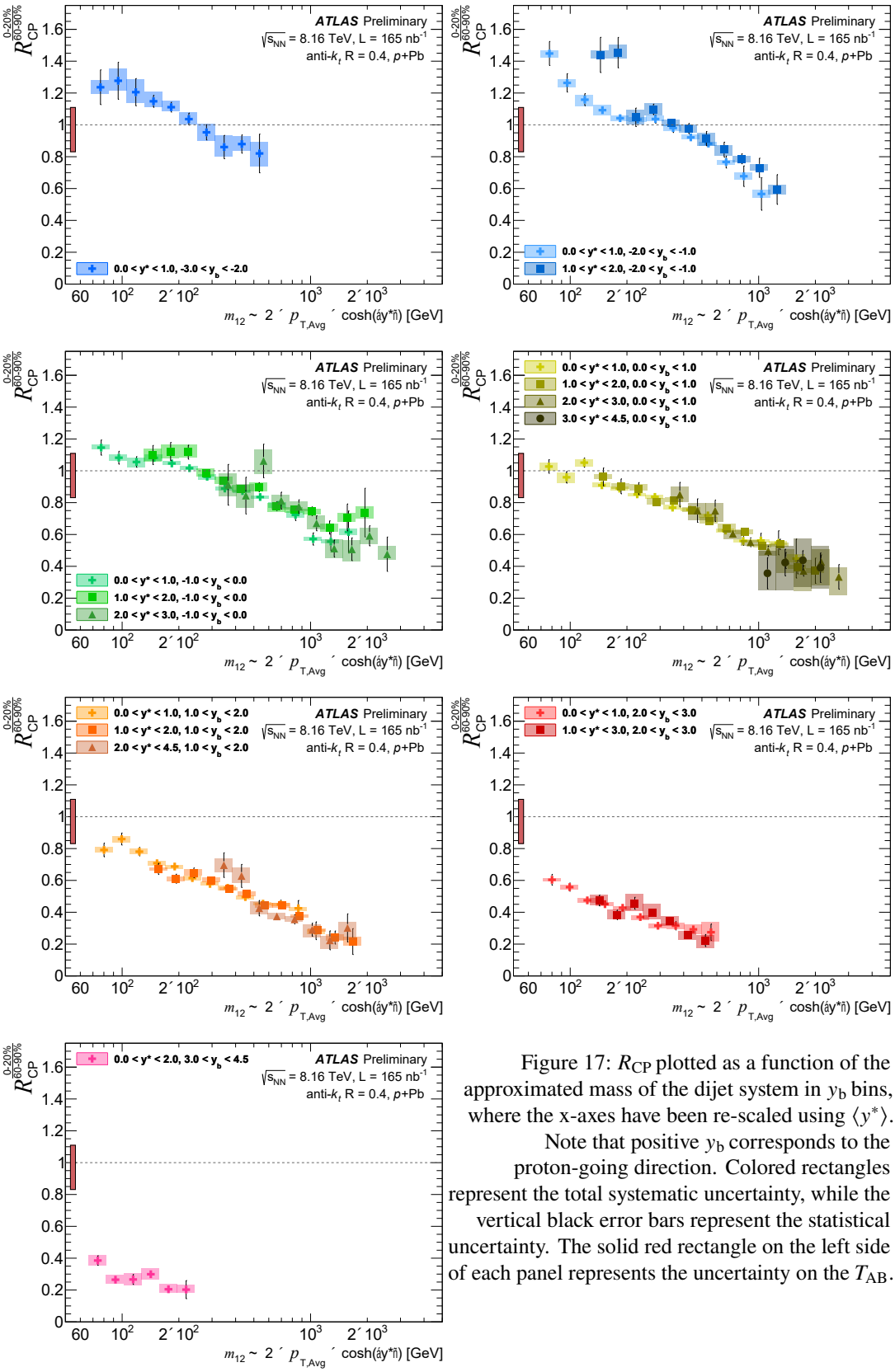

Figure 17: R_{CP} plotted as a function of the approximated mass of the dijet system in y_{b} bins, where the x-axes have been re-scaled using $\langle y^{*} \rangle$. Note that positive y_{b} corresponds to the proton-going direction. Colored rectangles represent the total systematic uncertainty, while the vertical black error bars represent the statistical uncertainty. The solid red rectangle on the left side of each panel represents the uncertainty on the T_{AB}.

7 Conclusion

This note presents the measurement of triple-differential per-event dijet yield centrality dependence in p+Pb collisions at $\sqrt{s_{\mathrm{NN}}}$ = 8.16 TeV over a wide kinematic range. The measured yield in central (0–20%) and peripheral (60–90%) p+Pb collisions are used to construct the R_{CP}, also reported in this note. The centrality of the p+Pb reaction was characterized using the transverse energy accumulated in the forward calorimeter ($3.2 < |\eta| < 4.9$) on the Pb-going side of the detector. The mean nuclear thickness function, T_{AB}, was evaluated for each centrality interval by making use of a Glauber Monte Carlo analysis.

Within the same (y_{b},y^*) bin, the per-event dijet yield results for both centrality selections show a decreasing trend with $p_{\mathrm{T,Avg}}$ that spans up to seven orders of magnitude. The yield also decreases with increasing dijet rapidity separation at comparable $p_{\mathrm{T,Avg}}$ and y_{b}.

The average value of the dijet boost system, $\langle y_{\mathrm{b}} \rangle$, and dijet half separation, $\langle y^* \rangle$, were used to display the R_{CP} results as a function of approximated kinematic variables representative of the partonic collision (x_p, x_{Pb}, m_{12}). The results of the measurement show a clear log-linear trend as a function of x_p, with the R_{CP} decreasing when accessing a higher partonic momentum fraction in the proton. A log-linear trend is observed also as a function of the approximated mass of the dijet system. The results suggest that such a behavior starts to break while approaching backward y_{b} bins, linked to events probing the valence region in the lead nucleus. A common suppression trend for the entire x_{Pb} range is observed as a function of x_p.

The results presented in this note represent the first investigation of suppression in p+Pb collisions via a triple-differential measurement of dijet production. By fully constraining the parton-level kinematics, the results provide new insights for the analysis of the physics governing the suppression of jet production in central p+Pb scatterings compared to peripheral ones. These results will help in further constraining theoretical models.

References

[1] J. L. Albacete et al.,
Predictions for Cold Nuclear Matter Effects in p+Pb Collisions at $\sqrt{s_{NN}} = 8.16\,TeV$,
Nucl. Phys. A **972** (2018) 18, arXiv: 1707.09973 [hep-ph] (cit. on p. 2).

[2] M. A. Al-Mashad et al.,
Dijet azimuthal correlations in p-p and p-Pb collisions at forward LHC calorimeters, (2022),
arXiv: 2210.06613 [hep-ph] (cit. on p. 2).

[3] R. A. Khalek,
Impact of LHC dijet production in pp and pPb collisions on the nNNPDF2.0 nuclear PDFs,
SciPost Phys. Proc. (2022) 135,
URL: https://scipost.org/10.21468/SciPostPhysProc.8.135 (cit. on p. 2).

[4] K. J. Eskola, I. Helenius, P. Paakkinen and H. Paukkunen,
Impact of dijet and D-meson data from 5.02 TeV p+Pb collisions on nuclear PDFs,
Nucl. Phys. A **1005** (2021) 121944, ed. by F. Liu, E. Wang, X.-N. Wang, N. Xu and B.-W. Zhang,
arXiv: 2001.10385 [hep-ph] (cit. on p. 2).

[5] H. Paukkunen, *Status of nuclear PDFs after the first LHC p–Pb run*,
Nuclear Physics A **967** (2017) 241, The 26th International Conference on Ultra-relativistic Nucleus-Nucleus Collisions: Quark Matter 2017, ISSN: 0375-9474,
URL: https://www.sciencedirect.com/science/article/pii/S0375947417301318
(cit. on p. 2).

[6] CMS Collaboration, *Constraining Gluon Distributions in Nuclei Using Dijets in Proton–Proton and Proton–Lead Collisions at* $\sqrt{s_{NN}} = 5.02\,TeV$, Phys. Rev. Lett. **121** (2018) 062002,
arXiv: 1805.04736 [hep-ex] (cit. on p. 2).

[7] ATLAS Collaboration, *Centrality and rapidity dependence of inclusive jet production in* $\sqrt{s_{NN}} = 5.02\,TeV$ *proton-lead collisions with the ATLAS detector*, Phys. Lett. B **748** (2015) 392,
arXiv: 1412.4092 [hep-ex] (cit. on pp. 2, 9, 11).

[8] PHENIX Collaboration, *Centrality-dependent modification of jet-production rates in deuteron-gold collisions at* $\sqrt{s_{NN}} = 200\,GeV$, Phys. Rev. Lett. **116** (2016) 122301,
arXiv: 1509.04657 [nucl-ex] (cit. on p. 2).

[9] M. Alvioli, L. Frankfurt, D. Perepelitsa and M. Strikman, *Global analysis of color fluctuation effects in proton– and deuteron–nucleus collisions at RHIC and the LHC*,
Phys. Rev. D **98** (2018) 071502, arXiv: 1709.04993 [hep-ph] (cit. on pp. 2, 11).

[10] A. Bzdak, V. Skokov and S. Bathe, *Centrality dependence of high energy jets in p+Pb collisions at energies available at the CERN Large Hadron Collider*, Phys. Rev. C **93** (2016) 044901,
arXiv: 1408.3156 [hep-ph] (cit. on pp. 2, 11).

[11] N. Armesto, D. C. Gülhan and J. G. Milhano,
Kinematic bias on centrality selection of jet events in pPb collisions at the LHC,
Phys. Lett. B **747** (2015) 441, arXiv: 1502.02986 [hep-ph] (cit. on pp. 2, 11).

[12] D. V. Perepelitsa and P. A. Steinberg, *Calculation of centrality bias factors in p+A collisions based on a positive correlation of hard process yields with underlying event activity*, (2014),
arXiv: 1412.0976 [nucl-ex] (cit. on p. 2).

[13] ALICE Collaboration,
Centrality dependence of particle production in p-Pb collisions at $\sqrt{s_{NN}} = 5.02$ *TeV*,
Phys. Rev. C **91** (2015) 064905, arXiv: 1412.6828 [nucl-ex] (cit. on p. 2).

[14] ATLAS Collaboration,
Measurement of the dependence of transverse energy production at large pseudorapidity on the hard-scattering kinematics of proton–proton collisions at $\sqrt{s} = 2.76$ *TeV with ATLAS*,
Phys. Lett. B **756** (2016) 10, arXiv: 1512.00197 [hep-ex] (cit. on pp. 2, 11).

[15] ATLAS Collaboration, *Dijet azimuthal correlations and conditional yields in pp and p + Pb collisions at* $\sqrt{s_{NN}} = 5.02$ *TeV with the ATLAS detector*, Phys. Rev. C **100** (2019) 034903,
arXiv: 1901.10440 [hep-ex] (cit. on p. 2).

[16] L. McLerran and R. Venugopalan,
Computing quark and gluon distribution functions for very large nuclei,
Phys. Rev. D **49** (5 1994) 2233,
URL: https://link.aps.org/doi/10.1103/PhysRevD.49.2233 (cit. on p. 2).

[17] ATLAS Collaboration, *Measurement of the centrality dependence of the charged-particle pseudorapidity distribution in proton–lead collisions at* $\sqrt{s_{NN}} = 5.02$ *TeV with the ATLAS detector*, Eur. Phys. J. C **76** (2016) 199, arXiv: 1508.00848 [hep-ex] (cit. on pp. 3, 5).

[18] M. L. Miller, K. Reygers, S. J. Sanders and P. Steinberg,
Glauber modeling in high energy nuclear collisions, Ann. Rev. Nucl. Part. Sci. **57** (2007) 205,
arXiv: nucl-ex/0701025 (cit. on p. 3).

[19] ATLAS Collaboration, *The ATLAS Experiment at the CERN Large Hadron Collider*,
JINST **3** (2008) S08003 (cit. on p. 4).

[20] ATLAS Collaboration, *The ATLAS Collaboration Software and Firmware*,
ATL-SOFT-PUB-2021-001, 2021, URL: https://cds.cern.ch/record/2767187 (cit. on p. 4).

[21] ATLAS Collaboration, *ATLAS Insertable B-Layer: Technical Design Report*,
ATLAS-TDR-19; CERN-LHCC-2010-013, 2010,
URL: https://cds.cern.ch/record/1291633 (cit. on p. 4),
Addendum: ATLAS-TDR-19-ADD-1; CERN-LHCC-2012-009, 2012, URL:
https://cds.cern.ch/record/1451888.

[22] B. Abbott et al., *Production and integration of the ATLAS Insertable B-Layer*,
JINST **13** (2018) T05008, arXiv: 1803.00844 [physics.ins-det] (cit. on p. 4).

[23] ATLAS Collaboration, *Operation of the ATLAS trigger system in Run 2*, JINST **15** (2020) P10004,
arXiv: 2007.12539 [hep-ex] (cit. on p. 4).

[24] ATLAS Collaboration, *Transverse momentum and process dependent azimuthal anisotropies in* $\sqrt{s_{NN}} = 8.16$ *TeV p+Pb collisions with the ATLAS detector*, Eur. Phys. J. C **80** (2020) 73,
arXiv: 1910.13978 [nucl-ex] (cit. on p. 5).

[25] B. Alver, M. Baker, C. Loizides and P. Steinberg, *The PHOBOS Glauber Monte Carlo*, (2008),
arXiv: 0805.4411 [nucl-ex] (cit. on p. 5).

[26] C. Loizides, J. Nagle and P. Steinberg, *Improved version of the PHOBOS Glauber Monte Carlo*,
SoftwareX **1-2** (2015) 13, arXiv: 1408.2549 [nucl-ex] (cit. on p. 5).

[27] GEANT4 Collaboration, S. Agostinelli et al., *GEANT4 – a simulation toolkit*,
Nucl. Instrum. Meth. A **506** (2003) 250 (cit. on p. 5).

[28] ATLAS Collaboration, *The ATLAS Simulation Infrastructure*, Eur. Phys. J. C **70** (2010) 823, arXiv: 1005.4568 [physics.ins-det] (cit. on p. 5).

[29] T. Sjöstrand et al., *An introduction to PYTHIA 8.2*, Comput. Phys. Commun. **191** (2015) 159, arXiv: 1410.3012 [hep-ph] (cit. on p. 5).

[30] ATLAS Collaboration, ATLAS-PHYS-PUB-2014-021, https://cds.cern.ch/record/1966419 (cit. on p. 5).

[31] R. D. Ball et al., *Parton distributions with LHC data*, Nucl. Phys. B **867** (2013) 244, arXiv: 1207.1303 [hep-ph] (cit. on p. 5).

[32] J. Bellm et al., *Herwig 7.1 Release Note*, (2017), arXiv: 1705.06919 [hep-ph] (cit. on p. 5).

[33] ATLAS Collaboration, *Strong constraints on jet quenching in centrality-dependent p+Pb collisions at 5.02 TeV from ATLAS*, (2022), arXiv: 2206.01138 [nucl-ex] (cit. on p. 6).

[34] ATLAS Collaboration, *Measurements of the suppression and correlations of dijets in Pb+Pb collisions at* $\sqrt{s_{NN}} = 5.02$ *TeV*, (2022), arXiv: 2205.00682 [nucl-ex] (cit. on p. 6).

[35] M. Cacciari, G. P. Salam and G. Soyez, *The anti-k_t jet clustering algorithm*, JHEP **04** (2008) 063, arXiv: 0802.1189 [hep-ph] (cit. on p. 6).

[36] M. Cacciari, G. P. Salam and G. Soyez, *FastJet user manual*, Eur. Phys. J. C **72** (2012) 1896, arXiv: 1111.6097 [hep-ph] (cit. on p. 6).

[37] ATLAS Collaboration, *Jet energy scale and its uncertainty for jets reconstructed using the ATLAS heavy ion jet algorithm*, ATLAS-CONF-2015-016, 2015, URL: https://cds.cern.ch/record/2008677 (cit. on p. 6).

[38] ATLAS Collaboration, *Measurement of inclusive jet and dijet production in pp collisions at* $\sqrt{s} = 7$ *TeV using the ATLAS detector*, Phys. Rev. D **86** (2012) 014022, arXiv: 1112.6297 [hep-ex] (cit. on p. 6).

[39] ATLAS Collaboration, *Jet energy scale measurements and their systematic uncertainties in proton–proton collisions at* $\sqrt{s} = 13$ *TeV with the ATLAS detector*, Phys. Rev. D **96** (2017) 072002, arXiv: 1703.09665 [hep-ex] (cit. on p. 7).

[40] G. D'Agostini, *A multidimensional unfolding method based on Bayes' theorem*, Nucl. Instrum. Meth. A **362** (1995) 487, ISSN: 0168-9002 (cit. on p. 7).

[41] T. Adye, 'Unfolding algorithms and tests using RooUnfold', *Proceedings, 2011 Workshop on Statistical Issues Related to Discovery Claims in Search Experiments and Unfolding (PHYSTAT 2011)* (CERN, Geneva, Switzerland, 17th–20th Jan. 2011) 313, arXiv: 1105.1160 [physics.data-an] (cit. on p. 7).

[42] ATLAS Collaboration, *Evaluating statistical uncertainties and correlations using the bootstrap method*, ATL-PHYS-PUB-2021-011, 2021, URL: https://cds.cern.ch/record/2759945 (cit. on p. 8).

[43] ATLAS Collaboration, *Jet energy scale and resolution measured in proton–proton collisions at* $\sqrt{s} = 13$ *TeV with the ATLAS detector*, Eur. Phys. J. C **81** (2020) 689, arXiv: 2007.02645 [hep-ex] (cit. on p. 9).

[44] ATLAS Collaboration, *Jet energy scale and its uncertainty for jets reconstructed using the ATLAS heavy ion jet algorithm*, (2015) (cit. on p. 9).